

Planar [Cu–S]–Organic Framework for Selective and Low-Overpotential CO₂ Reduction to Formate

Roohi, Khatereh; Soleimani, Mohammad; Khossossi, Nabil; Canossa, Stefano; Kosari, Ali; Mohseni Armaki, A.; Ahmadi, Majid; van der Veer, Ewout; Ramdin, Mahinder; Ravi Anusuyadevi, Prasaanth

DOI

10.1002/sstr.202500235

Publication date 2025

Document VersionFinal published version

Published in Small Structures

Citation (APA)

Roohi, K., Soleimani, M., Khossossi, N., Canossa, S., Kosari, A., Mohseni Armaki, A., Ahmadi, M., van der Veer, E., Ramdin, M., Ravi Anusuyadevi, P., Gonugunta, P., Mol, A., Dey, P., & Taheri, P. (2025). Planar [Cu–S]–Organic Framework for Selective and Low-Overpotential CO Reduction to Formate. *Small Structures*, *6*(10), Article 2500235. https://doi.org/10.1002/sstr.202500235

Important note

To cite this publication, please use the final published version (if applicable). Please check the document version above.

Copyright

Other than for strictly personal use, it is not permitted to download, forward or distribute the text or part of it, without the consent of the author(s) and/or copyright holder(s), unless the work is under an open content license such as Creative Commons.

Takedown policy

Please contact us and provide details if you believe this document breaches copyrights. We will remove access to the work immediately and investigate your claim.

www.small-structures.com

Planar [Cu-S]-Organic Framework for Selective and Low-Overpotential CO₂ Reduction to Formate

Khatereh Roohi, Mohammad Soleimani, Nabil Khossossi, Stefano Canossa, Ali Kosari, Seyedamirhossein Mohseni Armaki, Majid Ahmadi, Ewout van der Veer, Mahinder Ramdin, Prasaanth Ravi Anusuyadevi, Prasad Gonugunta, Arjan Mol, Poulumi Dey, and Peyman Taheri*

The development of advanced catalysts with innovative nanoarchitectures is critical for addressing energy and environmental challenges such as the electrochemical CO2 reduction reaction (CO2 RR). Herein, the synthesis of an innovative copper-sulfur planar structure, Cu-S-BDC, within a metal-organic framework (MOF) catalyst is presented, which demonstrates 100% selectivity toward formate as the sole carbon product. Structural analysis and surface characterizations reveal that Cu-S-BDC exhibits quasi-2D inorganic building units, with Cu bonded to two S-CH3 groups and one BDC linker, while carboxylate groups adopt a bridging coordination mode. This unique arrangement not only imparts remarkable structural stability but also enhances the electronic properties of the MOF, as evidenced by a narrow bandgap of 1.203 eV that facilitates efficient charge transfer and increased electrochemical current density in CO2RR. Notably, it offers a Faradaic efficiency of 92% for formate at an overpotential as low as $-0.4 \, \text{V}$ versus the reversible hydrogen electrode (RHE) in an aqueous electrolyte of 1 M KOH, as well as a current density of -25.8 mA cm² at -0.9 V versus RHE, averaged over 24 h of electrolysis. This study highlights a fresh perspective in the field of MOF electrocatalysts by demonstrating that engineering the metal coordination environment can significantly enhance the electronic properties and consequently improve the electrocatalytic performance of these materials.

1. Introduction

The increasing concentration of carbon dioxide (CO2) in the atmosphere raises significant concerns about our dependence on fossil fuels for energy generation. $^{[1,2]}$ Consequently, various strategies aimed at achieving a carbon-neutral footprint are being developed, including the exploration of environmentally friendly energy sources and carbon cycles as viable alternatives to fossil fuels.[3,4] Electrochemical carbon dioxide reduction reaction (CO2 RR) powered by renewable electricity offers a promising approach to convert CO₂ into valuable chemicals, simultaneously achieving carbon recycling and renewable energy storage. [5-7] However, CO₂RR often encounters some challenges such as production of a diverse array of products, necessitating supplementary separation or conversion processes. These additional incur added costs for both implementation and operation.[8] In this context, the design of efficient electrocatalysts capable of selectively converting CO2 into targeted products while maintaining a

K. Roohi, M. Soleimani, N. Khossossi, S. Mohseni Armaki, P. Ravi Anusuyadevi, P. Gonugunta, A. Mol, P. Dey, P. Taheri Department of Materials Science and Engineering Faculty of Mechanical Engineering Delft University of Technology Mekelweg 2, 2628 CD Delft, The Netherlands E-mail: p.taheri@tudelft.nl

S. Canossa Department of Chemistry and Applied Biosciences ETH Zürich Vladimir-Prelog-Weg 1, Zürich, Switzerland

The ORCID identification number(s) for the author(s) of this article can be found under https://doi.org/10.1002/sstr.202500235.

© 2025 The Author(s). Small Structures published by Wiley-VCH GmbH. This is an open access article under the terms of the Creative Commons Attribution License, which permits use, distribution and reproduction in any medium, provided the original work is properly cited.

DOI: 10.1002/sstr.202500235

A. Kosari Materials and Structural Analysis Division Thermo Fisher Scientific De Schakel 2, 5651 GH Eindhoven, The Netherlands

M. Ahmadi, E. van der Veer Zernike Institute for Advanced Materials University of Groningen Nijenborgh 4, Groningen, The Netherlands

M. Ramdin
Department of Process and Energy
Faculty of Mechanical Engineering
Delft University of Technology
Mekelweg 2, 2628 CD Delft, The Netherlands

www.advancedsciencenews.com



www.small-structures.com

high level of activity represents a significant research opportunity. $^{[9,10]}$

Commonly investigated CO₂ RR electrocatalysts in research include various metal-related substances such as metal oxides, metal alloys, bimetals, transition metals, metal chalcogenides, and metal–organic complexes.^[11–16] Pioneering investigations have shown that among all transition metals, copper-based electrodes exhibit the highest catalytic activity in converting CO₂ into valuable chemicals.^[17–19] Nevertheless, the selectivity of the reaction toward a specific product on copper-containing electrocatalysts remains considerably below the levels required for practical applications.^[20] The fundamental reason for the relatively limited selectivity of metallic copper catalysts is attributed to the linear relationship observed in the binding energies of the three primary CO₂ RR intermediates: *CO, *COOH, and *CHO.^[21,22]

Various material innovative strategies have been proposed to disrupt the linear scaling of intermediates on the surface of copper catalyst. A particularly promising approach is ensemble control, which entails identifying the smallest active site and its surrounding space essential for the desired reaction, and then deliberately tailoring it. [23] In this regard, theoretical and experimental research suggest that p-block elements, such as sulfur, could contribute to $\rm CO_2$ bond formation on electrocatalyst surfaces, potentially disrupting the linear scaling relationships observed for metals. [24] Specifically, Cu—S bonds could influence the binding strength of *HCOO and *COOH intermediates by suppressing the key intermediate of the hydrogen evolution reaction (HER), i.e., *H, ultimately favoring the formation of the target $\rm CO_2$ RR product, formate. [25–27]

While the atomically precise incorporation of selectivity modifiers into the metallic-based catalysts is challenging, metal-ligand complexes, such as metal-organic frameworks (MOFs), offer exceptional structural tunability, making them ideal materials for this purpose. Additionally, MOFs provide porosity and a large surface area, further enhancing their suitability for electrocatalyst applications. [28-31] Despite these advantages, the utilization of MOFs in electrocatalyst applications has been limited by their poor conductivity, resulting in low current density. [32] This limitation primarily stems from the use of carboxylate linkers in constructing multidimensional structural frameworks. The high electronegativity of the oxygen atoms in these carboxylates increases the potential required for electron passage through the organic linkers.^[33] Consequently, there is a diminished overlap between the oxygen atoms and the metal d-orbitals, leading to the low electrical conductivity observed in most reported MOFs.^[34]

To address this issue, incorporating metal–sulfur bonds improves the electrical conductivity of the MOF due to the strong overlap between the sulfur p-orbitals and the metal d-orbitals, facilitating efficient charge transfer through chemical bonds. Notably, in multidimensional MOFs, the planar metal–sulfur bond formed through a chain network demonstrates anisotropic behavior, restricting charge transport to a single dimension and thereby enhancing the conductivity. In particular, a 2D building unit of these planar metal–sulfur bonds within the MOF structure facilitates charge transfer, consequently enhancing overall conductivity. $^{[35-39]}$

As a result, incorporating planar Cu—S bonds into the MOF structure offers benefits in two critical aspects of CO₂ RR. First, it selectively promotes the formation of a single product during

CO₂ RR by disrupting the linear scaling of intermediates. Second, its high conductivity enhances the electrochemical reduction current density due to facile charge transfer. Consequently, our study delves into the structural tuning of copper benzenedicarboxylic acid MOF, (Cu-BDC-MOF), by incorporating sulfur into the framework in a controlled manner, resulting in the formation of the Cu-S-BDC structure. The resulting enhanced MOF exhibits a thin flake morphology with planar Cu-S building units, which serve as catalytically active sites for selective CO₂ RR toward formate production. To the best of our knowledge, our synthesized Cu-S-BDC MOF is the only Cu-based MOF electrode capable of selectively producing formate at such low overpotential and high current density. It is worth noting that we achieved this in an aqueous medium, eliminating the need for the ionic liquids often used in selective conversion processes for MOFs—an approach that can undermine the sustainability of CO₂ electrolysis. [40] Moreover, this work, supported by experimental and theoretical evidence, marks a significant accomplishment in designing highly conductive and selective MOFs paving the way for the rapid development of novel and highly efficient crystalline materials for CO2 RR applications.

2. Results and Discussion

2.1. Design, Synthesis, and Crystal Structure Determination

With the primary objective of introducing sulfur into the structural composition of Cu–BDC, dimethyl sulfoxide solvent (DMSO) together with Cu(II) salt and BDC linker was defined as precursors. Using the ab initio USPEX method, the optimized Cu–S–BDC MOF candidates were generated (**Figure 1a**). The most optimized MOF structure candidates, I and II, are shown in Figure 1b. As aimed, the high feasibility of sulfur binding with Cu is exhibited in 1b-(I). The prospective cell parameters of both structures are listed in Table S1, Supporting Information. Also, the Cu–S, C–H, C–S, and C–O bond lengths in the predicted structure are equal to 2.2305, 1.093, 1.820, and 1.275 Å, respectively.

Accordingly, Cu-S-BDC MOF was synthesized in DMSO solvent as schematically shown in Figure S2, Supporting Information, resulting in the formation of a green-colored, rectangular, thin sheet of crystalline Cu-S-BDC MOF (Figure 2a). This differs from the conventional Cu-BDC MOF synthesized in dimethylformamide (DMF) solvent, which typically displays a thicker plate morphology, as previously reported. [41] The formation mechanism of Cu-S-BDC MOF could be explained through the reaction of Cu(II) salt with decomposed DMSO in the presence of BDC linker. At a temperature of 14 °C, DMSO undergoes decomposition to form thiol (RSH), [42] which serves as a reducing agent. Due to the excess amount of DMSO in the precursor mixture, Cu²⁺ ions are reduced by S-CH₃ compounds to Cu⁺, which initially react with the thiols. Subsequently, the BDC linker becomes engaged in the reaction, occupying the remaining coordination sites of Cu⁺.

Energy-dispersive spectroscopy (EDS) analyses of Cu–S–BDC MOF sample confirm the distribution of S, C, O, and Cu (Figure S3, Supporting Information). Moreover, Fourier-transform

2688462, 2025, 10, Downloaded from https://onlinelibrary.wiley.com/doi/10.1002/sstr.2025090235 by Techical University Delft, Wiley Online Library on [20/10/2025]. See the Terms and Conditions (https://onlinelibrary.wiley.com/erms-and-conditions) on Wiley Online Library for rules of use; OA articles are governed by the applicable Creative Commons License

www.small-structures.com

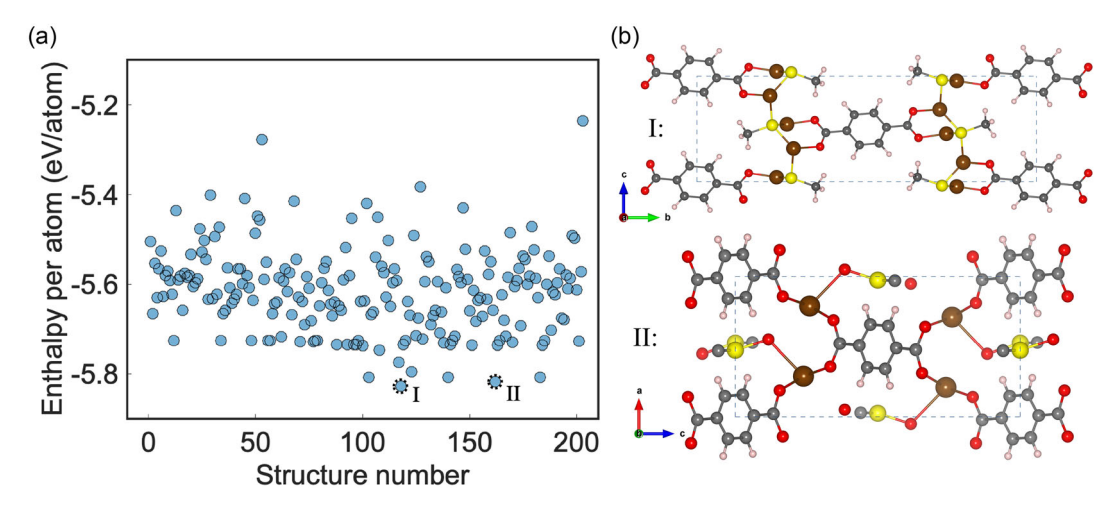


Figure 1. Design: a) USPEX evolutionary crystal structure prediction of Cu-S-BDC MOF, showcasing the enthalpy per atom of all candidate crystal structures along the evolutionary trajectory. A dashed black circle denotes the first occurrence of the final global minimum, representing the lowest energy unit cell predicted for Cu-S-BDC MOF. b) Two lowest energy unit cells of Cu-S-BDC MOF, with structure "1" being more probable due to its slightly lower energy. The color scheme represents Cu (brown), S (yellow), C (grey), O (red), and H (pink) atoms.

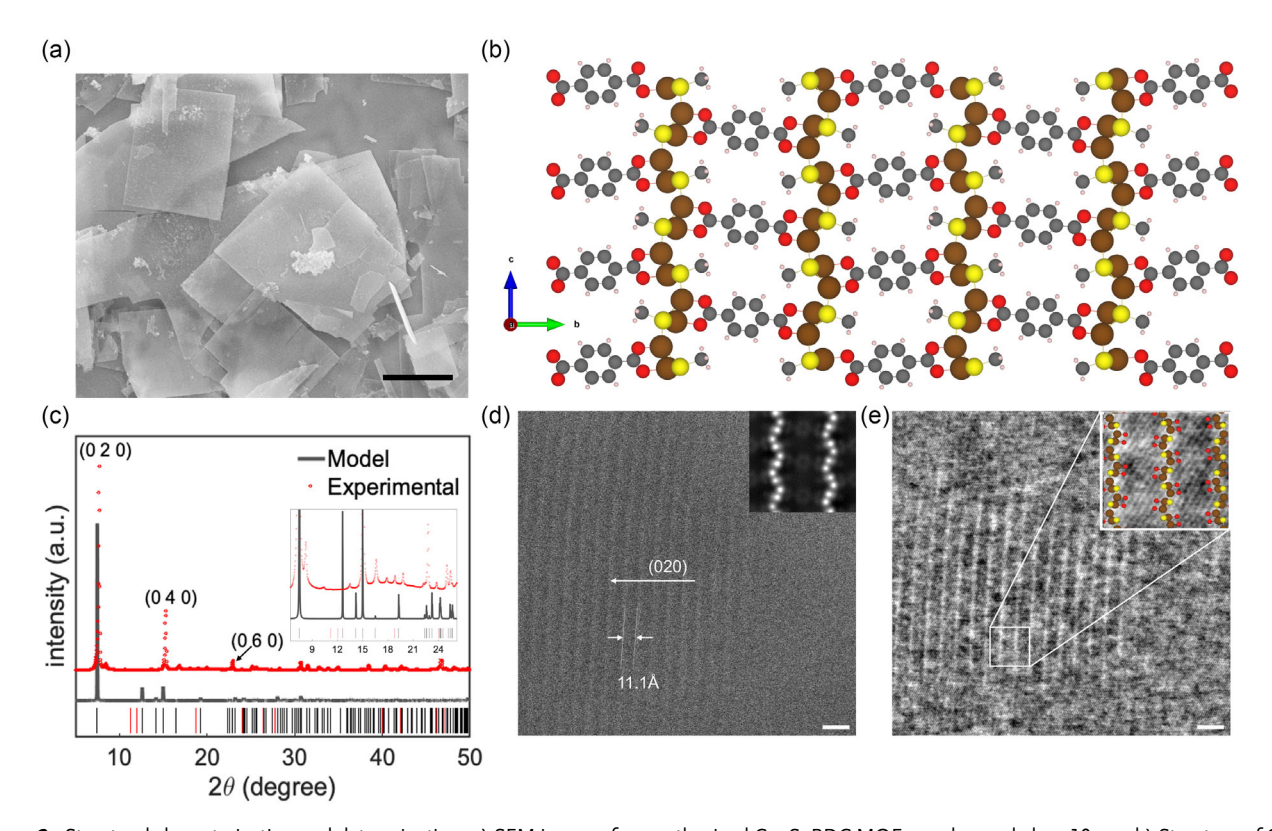


Figure 2. Structural characterization and determination: a) SEM image of as-synthesized Cu-S-BDC MOF powder; scale bar: 10 µm. b) Structure of Cu-S-BDC MOF rendered based on the SCXRD data exhibiting the formation of (-Cu-S-) plane along the c axis. The color scheme represents Cu (brown), S (yellow), C (gray), O (red); c) PXRD patterns of Cu-S-BDC MOF powder obtained from the experiment in red and model in black. Reflection positions are indicated by black and red ticks below the main plot, where black lines represent observed reflections and red lines denote missing reflections. d) HAADF-TEM image of the Cu-S-BDC showing the main plane of the MOF crystal (020) with d-spacing 020 of 11.1 Å. Scale bar: 2 nm. Inset: simulated HAADF-TEM of [1 0 0] direction, perpendicular to (020) planes. e) STEM-TEM image of the same zone as (d). Scale bar: 2 nm. Inset: zoomed-in image of the area within the white square, including the MOF structure at [1 0 0] direction.

www.small-structures.com

infrared spectroscopy (FTIR) of the synthesized MOF (Figure S4, Supporting Information) indicates the presence of Cu-S bond demonstrated by the peak at 823 cm⁻¹, [43] whereas as the highlighted peaks at 1294 and 1316 cm⁻¹ are attributed to C-H vibrations originating from DMSO. Thermogravimetric analysis (TGA) and mass spectrometry (MS) were conducted to identify the compounds released from the MOF at elevated temperatures and to evaluate its thermal stability (Figure S5, Supporting Information). The analysis confirms the presence of sulfur-containing compounds, as these compounds are observed to decompose and exit when the temperature reaches 32 °C. The TGA profile of Cu-S-BDC MOF suggests that the MOF is stable up to 30 °C. However, beyond this temperature, the MOF undergoes significant decomposition, concurrent with the simultaneous breakage of Cu-O and Cu-S bonds, as indicated by online MS measurements. The observed decomposition of the BDC linker aligns well with the reported decomposition temperature. [44] It is also observed from the pore size distribution plot from BET measurements (Figure S6, Supporting Information) that the effective pore size of the MOF is 3.95 nm. This is almost 10 times bigger than the kinetic diameter of CO₂ molecule, 3.3 Å, which assures the diffusion of CO₂ into the pores for further reaction at the active sites.^[45]

Reciprocal space reconstructed of Cu-S-BDC MOF obtained from single-crystal X-ray diffraction (SCXRD) are shown in Figure S7, Supporting Information. Four different twins were identified in the data. One major component accounted for around 61% of the harvested maxima. Separate twin indexing results are listed in Supporting Information under SCXRD section. The obtained crystalline structure from SCXRD, represented in Figure 2b, with unit cell parameters of a = $3.98762 \,\text{Å}, \, b = 7.5698 \,\text{Å}, \, \text{and} \, \, c = 23.5895 \,\text{Å}, \, \text{is in line with}$ the structure from density functional theory (DFT) optimization indicating a quasi-2D inorganic building unit in the MOF structure. It is observed that the structural parameters of the predicted Cu-S-BDC MOF (I) configuration closely match the experimentally obtained data, exhibiting minor variations ranging from a decrease of $\approx 0.27\%$ to an increase of up to 1.26%.

As per the structural analysis derived from SCXRD, Cu-S-BDC MOF forms in the P21/c space group, featuring unit cells containing five Cu⁺ cations (Table S2, Supporting Information). Each Cu⁺ cation displays a trigonal coordination environment with two S-CH₃ from reduced DMSO and an oxygen atom from the BDC linker. The higher concentration of DMSO in the synthetic mixture results in increased presence of sulfur-containing compounds in the Cu coordination environment. Therefore, as it can be seen in the structure in Figure 2b, carboxylate groups in the BDC linker exhibit bridging coordination mode for the chain of Cu-S-CH₃ formed roughly along the c axis. Thus, the synthesized MOF represents a novel Cu-S-BDC MOF framework featuring a quasi-2D inorganic building unit.

The average structure model derived from SCXRD was utilized for a subsequent powder X-ray diffraction (PXRD) simulation. As depicted in Figure 2c, the simulation closely aligns with the experimental PXRD data obtained from Cu-S-BDC MOF powder, indicating a high level of agreement. The observed shifts in peak positions, especially pronounced at higher angles of 2θ , can be attributed to the SCXRD data collection conducted at 100 K. Any additional peaks observed could stem from impurities or structural alterations occurring at low temperatures. The main PXRD peaks correspond to d-spacings of 11.5, 5.8, and 3.9 Å, which are associated with the (0n0) planes as indicated in the graph.

The high crystallinity of the MOF powder is evident in both the high-angle annular dark-field transmission electron microscopy (HAADF-TEM) and scanning transmission electron microscopy (STEM) images depicted in Figure 2d,e. Due to the presence of organic components, the sample displays sensitivity to damage induced by the electron beam. Nonetheless, measured d-spacing, shown in Figure 2d, is in good agreement with the d-spacing of the (020) planes. Moreover, the simulated HADDF image of the structure mirrors the pattern observed in the experimental image. The atomic arrangement of Cu-S-BDC MOF along the [1 0 0] direction, perpendicular to (020) planes, is also depicted in the inset of Figure 2e. Notably, the lines depicted in the STEM image correspond to the O-Cu-S chain. Another orientation of the crystal was also investigated using STEM, perpendicular to the (031) planes with *d*-spacing of 5.6 Å. Figure S9, Supporting Information, represents zone [0 7 -20] of the Cu-S-BDC crystal and O-Cu-S planes are well visible.

The Raman spectrum (Figure 3a) exhibits peaks at 438 and 272 cm⁻¹, corresponding to Cu–S, [46] which further confirms the formation of crystal I, generated by DFT optimization shown in Figure 1b(I). The peaks observed at 98 and 141 cm⁻¹ are associated with the Cu-O bonds, while the remaining peaks indicated in the graph in black originate from the BDC

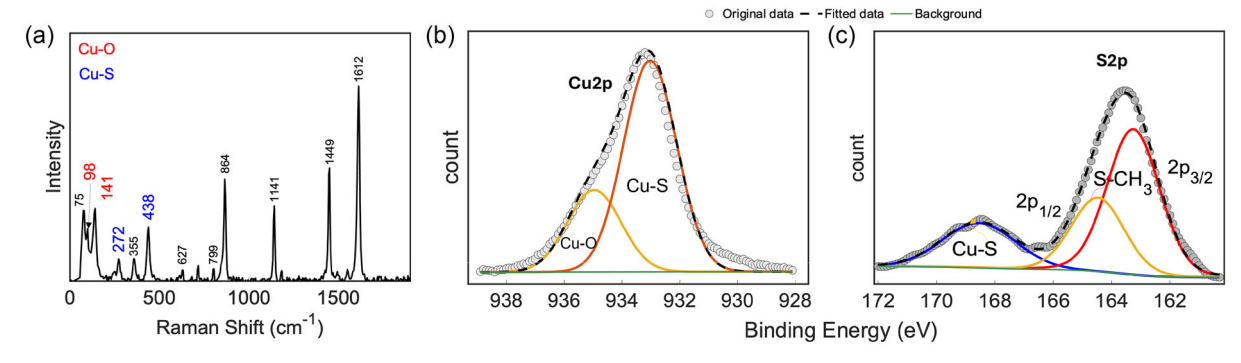


Figure 3. Surface characterization: a) the Raman spectrum of Cu-S-BDC MOF XPS high-resolution b) Cu 2p and c) S 2p spectra with peak fittings, labeled with the corresponding bonds. The dashed curve represents the sum of fitted peaks, and the gray dots are the measured peaks.

of use; OA articles are governed by the applicable Creative Commons I

SMQII ____ structure

www.advancedsciencenews.com www.small-structures.com

linker. [47,48] Additionally, X-ray photoelectron spectroscopy (XPS) survey shows the expected elements only, i.e., Cu, C, O, and S (Figure \$10a, Supporting Information). High-resolution XPS results of Cu 2p (Figure 3b) show Cu $2p_{3/2}$ subpeak at 933.1 eV attributed to Cu-bonding with S-CH₃, [49] whereas the peak at 935.3 eV corresponds to Cu-bonding to BDC linker through oxygen. [44] The subpeak area ratios of Cu-S/Cu-O are calculated to be 71.91/28.08 = 2.56, which closely matches the expected coordination environment of Cu within the MOF structure. A small shift of 0.5 eV for both subpeaks to higher binding energies suggests the charging effect induced by the presence of organic linkers. On the other hand, the S 2p spectrum (Figure 3c) displays two main peaks, confirming sulfur bonding with a metal, i.e., Cu, appearing at higher binding energies. The peak at 163.6 eV represents both $2p_{3/2}$ and $2p_{1/2}$ signals of S-CH₃, [50] Notably, the C-S interaction can also be discerned in the C 1s spectrum (Figure S10b, Supporting Information).

2.2. Electrochemical Characterizations, Product Analysis, and Reaction Mechanism

The electrocatalytic performance of the Cu–S–BDC MOF was assessed using linear sweep voltammetry (LSV) in a 1 M aqueous KOH electrolyte within a flow cell setup (Figure S4a, Supporting Information). Additionally, LSV results for conventional Cu–BDC are presented in **Figure 4**a for a comparison. LSV measurements were conducted in saturated electrolytes within the potential range of 0.5 to -1 V versus the reversible hydrogen electrode (RHE). It can be seen that the Cu–S–BDC MOF presents a more cathodic activity than Cu–BDC, favoring reduction reactions. Notably, an increase in the reductive current density of the

Cu-S-BDC MOF under a CO2 atmosphere, compared to that under an Ar atmosphere, becomes evident starting from 0 V versus RHE. As previously reported, [20] the standard reduction potential for CO₂RR products generally begins around 0.2 V versus RHE, while the reduction of CO2 to formate in an alkaline environment occurs at approximately +0.2 V versus RHE. This aligns with the observed activity of the Cu-S-BDC catalyst at lower potentials. A comparison of the LSV results of Cu-S-BDC MOF obtained in Ar- and CO₂-saturated gases indicates an overpotential of -0.46 V versus RHE for the Ar-saturated one, attributed to the hydrogen evolution reaction, whereas Cu-S-BDC MOF can convert CO2 at lower potentials. Furthermore, LSV graphs of Cu-S-BDC generally exhibit significantly higher catalytic activity compared to Cu-BDC MOF, attributable to higher conductivity. To dive further into the electrical properties of the proposed Cu-S-BDC MOF structure, electrochemical impedance spectroscopy (EIS) measurements were conducted in CO2-saturated 1 M KOH for both Cu-S-BDC and Cu-BDC MOFs at OCP. Figure 4b shows a lower charge transfer resistance (R_{ct}) of ${\approx}40\,\Omega$ for Cu–S–BDC compared to that of Cu–BDC appearing around 60 Ω , indicating an improved conductivity due to the incorporation of sulfur in the form of Cu-S planes.

Furthermore, the electronic band structure of Cu–S–BDC MOF was computed and depicted in Figure 4c. The calculated electronic bandgap is estimated through the energy difference between the valence band maximum (VBM) and the conduction band minimum (CBM). The computed band structure indicates that the narrowest electronic bandgap is 1.203 eV which occurs at the Γ (VBM) and X (CBM) points (gray dots in Figure 4c). It is noteworthy that semiconductor MOFs typically exhibit flat band lines, [51–57] characterized by bands with less than 0.05 eV dispersion widths, due to minimal orbital overlap caused by weak

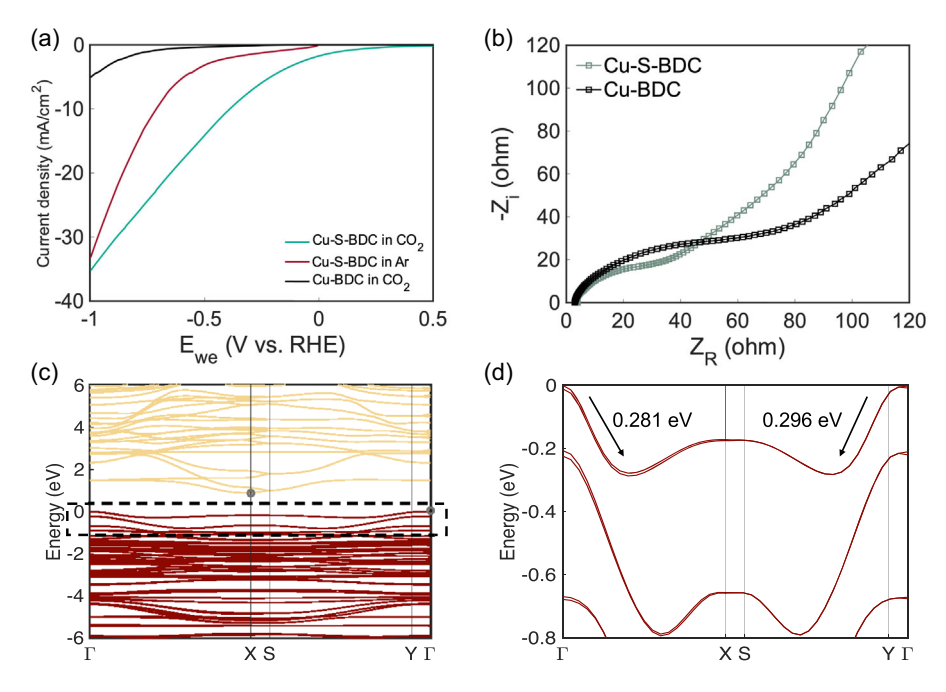


Figure 4. Electrochemical performance: a) LSV performance of the Cu–S–BDC MOF in Ar and CO₂ and Cu–BDC in CO₂ in 1 M KOH in a flow cell, with a scan rate of 50 mV s⁻¹. b) EIS Nyquist plots of Cu–S–BDC and Cu–BDC MOFs obtained in CO₂-saturated 1 M KOH solution. c) Electronic band structure and d) an expanded plot within the black dashed box in (c) showing the steep dispersion of the valence bands.

www.advancedsciencenews.com www.small-structures.com

hybridization of the orbitals in the metal nodes and organic linkers. However, the synthesized Cu-S-BDC MOF exhibits a unique band structure with a marked steep dispersion, as indicated in Figure 4d. Specifically, the VBM shows a relatively flat trend along the X–S and Y– Γ paths, but a steep decline along the Γ -X and -YS directions. The energy differences at the VBM between Γ -X and Y-S are 0.281 and 0.296 eV, respectively, as shown in the expanded Figure 4d. [52,54,58] The steep dispersion in the VBM is a clear sign of the unique charge transport properties, in particular, the extraordinary conductivity along $\Gamma - X$ and Y-S directions compared to other directions of the Cu-S-BDC MOF. This observation provides compelling evidence that higher conduction values occur in the direction along the Cu-S plane. Specifically, as the dispersion deviates from a flat profile to a sudden steep decrease, the effective mass of charge becomes lighter, consequently enhancing hole mobility and increasing electrical conductivity.

The analysis of total and partial density of states (DOSs), as depicted in Figure S12a, Supporting Information, indicates that both valence and conduction bands are composed of states from Cu, C, H, O, and S atoms. The orbital-decomposed density of state data reveals that the VBM largely consists of the states of Cu atoms with 3d orbital, with some contributions from the states of S (3p orbital), and with nearly negligible contributions from states of the other elements in the ligand. Moreover, the CBM predominantly consists of carbon atom states, with a minor contribution from oxygen atoms, and even less from copper and sulfur atoms. Hydrogen atoms have an almost negligible impact on both the VBM and CBM near the Fermi energy level. We have also provided the band-decomposed partial charge density for the VBM and CBM in Figure S12b,c, Supporting Information. These plots reveal that the VBM is primarily formed by the states of Cu and S, with the Cu-S plane providing a dense route for charge conduction.

The flow cell shown in Figure S11, Supporting Information, coupled with gas chromatography (GC) was used to analyze the CO₂RR products of the Cu-S-BDC MOF catalyst. The measurements were conducted at different applied potentials between -0.4 and -1 V versus RHE in CO₂-saturated 1 M KOH solution, at room temperature and under atmospheric pressure. Cu-S-BDC MOF shows selectivity toward formate only in all studied potentials (Figure 5a) whereas H₂ is the sole detected gas product (Figure S13, Supporting Information). The highest Faradaic efficiency (FE) of Cu–S–BDC MOF for formate is 92% \pm 7.3% at a relatively low overpotential of $-0.4 \,\mathrm{V}$ versus RHE. This result is close to what has been reported for Pb-based catalysts, which are well known for formate production.^[59] In contrast, metallic copper in various polycrystalline nanostructures deposited on GDEs, under the same potential range and electrolyte conditions, has been reported to produce a variety of gas and liquid products, including CH₄, C₂H₂, and others. [60] The results also reveal that the partial current density (PCD) of formate increases with the cathodic overpotential, thereby corroborating the findings of the LSV results depicted in Figure 4a. Specifically, at more cathodic potentials, the current responses of the catalyst in different media tend to converge, as water molecules increasingly engage with the active sites and drive higher HER. Conversely, the maximum PCD observed for formate is -19.2 mA cm^{-2} at the potential of -0.9 V versus RHE, which subsequently decreases at -1 V versus RHE.

The stability of the catalyst was also investigated with chronoamperometry (CA) for 24 h at a constant potential of −0.9 V versus RHE in 1 M KOH (Figure S14a, Supporting Information). The recorded current of $-25.79 \,\mathrm{mA} \,\mathrm{cm}^{-2}$ remained relatively constant over 24 h, indicating no significant deterioration or poisoning of the active sites during the measurement period. In addition, the morphology and elemental composition of the catalyst after long-term CA measurement remained

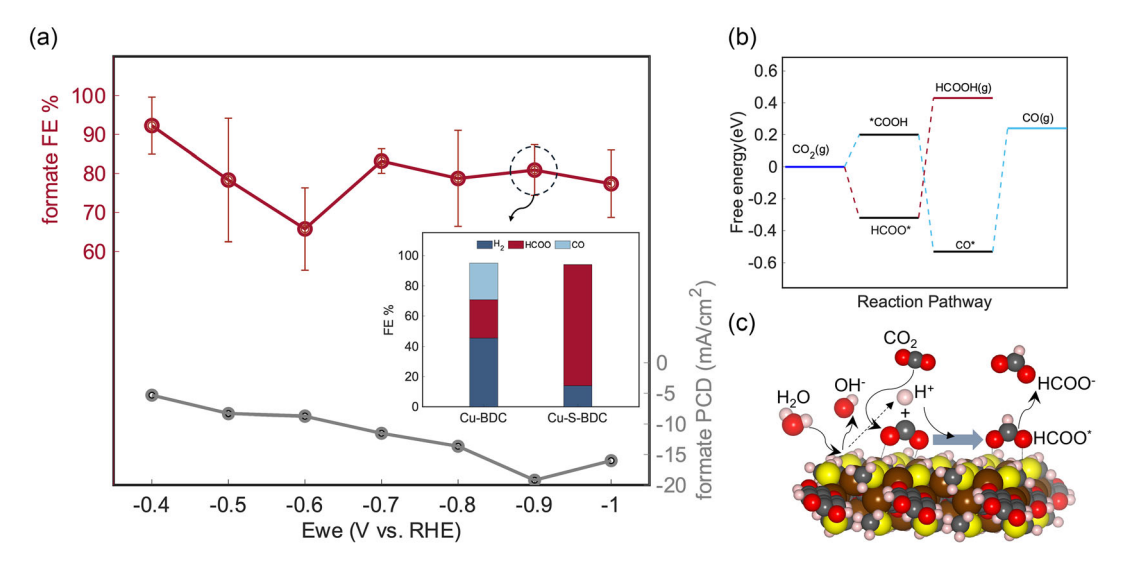


Figure 5. Product analysis. a) FE of Cu-S-BDC MOF powder deposited on GDE substrate in different potentials vs RHE. The black line shows the trend of the partial current density. Inset: Calculated FE values of Cu-BDC and Cu-S-BDC MOFs. The measurements were performed at -0.9 V versus RHE in 1 M KOH under CO_2 flow. b) The reaction pathway for CO and HCOOH formation on Cu–S–BDC MOF surface in the absence of an external potential (U =0 eV). Dashed red and blue lines are representative of the formate and carbon monoxide production pathways, respectively. c) Schematic CO2 RR mechanism illustrating on the surface of Cu-S-BDC through HCOO* intermediate.



www.advancedsciencenews.com www.small-structures.com

unchanged (Figure S14b,c, Supporting Information). The XRD spectrum of the Cu-S-BDC crystal remains the same after CA measurement at -0.9 V versus RHE, which is an additional demonstration of the stability of the MOF structure following electrochemical reaction. This indicates that by integrating the BDC linker into the coordination environment of Cu, we have successfully stabilized the Cu(I)-S active sites under the potential, extending stability. This is a key benefit of embedding the Cu(I)—S planes as catalytic active sites within the MOF structure, compared to non-MOF structures, generally exhibiting a lower stability. In this case, Cu-S-BDC MOF demonstrates the highest stability among Cu-S-based electrocatalysts, to the best of our knowledge (See Table S3, Supporting Information)

Furthermore, as illustrated in Figure S15, Supporting Information, no carbon products were observed when an Ar flow was used instead of CO₂. This confirms that the organic linker remains stable at the studied cathodic potential and the detected formate is not a result of BDC decomposition. The trend of averaged FE(COOH) and FE(H2) over time from different product analysis trials (Figure S16, Supporting Information) at constant potentials of -0.4 and -0.9 V versus RHE indicates that the majority of formate production occurs within the first 10 min of the reaction. This can be attributed to the initially high concentration of CO₂ molecules and the surface saturation of active sites, which gradually diminishes as the reaction proceeds. Additionally, continuous formation of formate, a liquid product that remains dissolved in the electrolyte reservoir, can gradually lead to electrolyte saturation and potentially shift the local reaction equilibrium, thereby hindering further formate production. Notably, given the proven evidence of catalyst stability (Figure S14, Supporting Information), the observed drop in FE(COOH) is mirrored by an equivalent rise in hydrogen FE at both potentials, strongly suggesting that flooding in the GDE-based electrolyzer reduces CO2 availability at the catalyst surface, as previously reported. [6,61] Inset of Figure 5a presents a comparison of the CO₂RR products of Cu-S-BDC and Cu-BDC MOFs. While Cu-S-BDC MOF shows a FE (HCOO-) of \approx 80%, Cu-BDC MOF has a total FE of 49%, divided into FE(HCOO⁻) of 25% and FE(CO) of 24%. This represents a substantial improvement in formate selectivity for Cu-S-BDC MOF. highlighting the crucial role of sulfur in the coordination environment of copper. A review of state-of-the-art Cu-based MOFs (summarized in Table S4, Supporting Information) shows that our synthesized Cu-S-BDC is the only formate producing MOF in aqueous CO₂ RR, highlighting its unique electrocatalytic performance.

To further elucidate the underlying CO₂RR mechanism, we constructed models and performed DFT calculations to evaluate the reaction energies on the Cu-S-BDC MOF. Previous studies have proposed two possible pathways for formate production: one proceeding through the HCOO* intermediate and the other via COO* combined with adsorbed H* on the surface. [20,62-64] Upon CO2 adsorption onto the Cu-S-BDC surface, the initial concerted proton-electron transfer (CPET) step can yield two distinct intermediates—HCOO*, in which CO2 binds through an oxygen atom, or *COOH, in which it binds through a carbon atom (Figure S17, Supporting Information). The subsequent CPET step leads to the formation of either HCOOH from HCOO* or CO from *COOH.

As shown in Figure 5b, the Cu–S–BDC catalyst surface favors the formation of the HCOO* intermediate, thus inhibiting the *COOH pathway. The free-energy diagrams in Figure 5b clearly indicate that HCOO* is the key intermediate for formate production. The potential-limiting step is identified as the second CPET process—conversion of HCOO* to HCOOH—with a calculated theoretical overpotential of 0.27 V. The optimized structure of Cu-S-BDC with the HCOO* intermediate (Figure S18, Supporting Information) shows that the CO₂ molecule is adsorbed onto the surface through both of its oxygen atoms. Additionally, the formation of CO is hindered by the strong binding affinity of CO to the Cu-S-BDC surface, evidenced by a binding energy of -0.79 eV (Figure S19, Supporting Information). To better understand the influence of the copper–sulfur bond on the reaction mechanism, we also investigated the CO₂ RR pathway on Cu-S-BDC structure II (Figure 1b), which features a reduced concentration of sulfur and a rearranged configuration of Cu and S atoms. As demonstrated in Figure S20a, Supporting Information, the binding strength of H* on the Cu atoms is increased in this configuration, thereby limiting the CPET step required for formate production. Our computational results indicate that the formation of both formate and CO is thormodynamically favorable on the Cu-S-BDC -II MOF (Figure S20b, Supporting Information) while strong binding of H* to the Cu atoms in structure II makes the formation of HCOOH challenging. Conversely, in our synthesized Cu-S-BDC MOF, the presence of sulfur in the Cu coordination environment results in weaker hydrogen binding on the catalyst surface, thus promoting favorable conditions for formate formation.

3. Conclusions

We have redesigned the structure of Cu-BDC MOF by introducing sulfur into its framework. The resulting Cu-S-BDC MOF features a planar structure of Cu-S units, exhibiting excellent selectivity for formate production as the sole detectable carbon product in a wide potential range. In contrast, Cu-BDC MOF produces both formate and carbon monoxide. The mechanism underlying this improvement involves a higher occupancy of Cu coordination sites by sulfur, as opposed to carbon, resulting in increased selectivity. Additionally, compared to Cu-BDC MOF, Cu-S-BDC MOF demonstrates improved current density, thanks to its planar Cu-S structure, as quasi-2D inorganic building units, that facilitate charge transfer. Our findings highlight the potential of MOFs as atomically dispersed electrocatalysts for CO₂RR, demonstrating their capacity to simultaneously enhance both selectivity and conductivity, the latter having traditionally been a limiting factor in their applications in electrochemical processes.

4. Experimental Section

Chemicals: Copper(II) nitrate (Cu(NO₃)₂.3H₂O, 99.999%), benzenedicarboxylic (C₈H₆O₄), dimethyl sulfoxid (99.999%), dimethylformamide (99 999%), isopropanol, and KOH all were purchased from Sigma-Aldrich. Polytetrafluoroethylene 55wt% dispersion in water was obtained from FUELCELL store. An ultrapure purification system (Milli-Q advantage A10) produced the deionized water purification system (19.2M cm) used



www advancedsciencenews com

www.small-structures.com

to make the solutions. The gas diffusion electrodes (GDE) from FUELCELL store were cut to $6.76\,\mathrm{cm^2}$ and used as substrates for $\mathrm{CO_2}$ RR electrochemical measurements

MOF Synthesis: For the synthesis of Cu–S–BDC MOF, Cu(NO₃)₂, and Terephthalic acid were combined in a 1:2 molar ratio, followed by the addition of 30 mL of DMSO. The mixture underwent stirring for 30 min to ensure complete dissolution of the precursors. Subsequently, the homogeneous mixture was carefully transferred to a 50 mL Teflon-lined stainless steel autoclave, sealed with Teflon tape. The sealed autoclave was then placed in an oven and heated to 14 °C for 24 h. Once the reaction concluded, the autoclave was cooled to room temperature and the resulting MOF crystals were collected using filter paper. To eliminate any residual unreacted precursors, the collected crystals underwent multiple wash cycles with DMSO and DMF. Finally, the washed crystals were air-dried at room temperature.

Electrode Preparation: Dried Cu–S–BDC and Cu–BDC MOF powders were mixed with PTFE (4:1 w%) in a water and isopropanol solution (1:1 vol%) to form an ink with an active material concentration of 5 mg mL⁻¹. The ink was then drop-cast onto GDE (catalyst loading of 1.5 mg cm²) using a pipette and dried under ambient air.

Characterization of Materials: PXRD was carried out with a Bruker D8 Advance diffractometer X-ray powder diffractometer equipped with a Cu-sealed tube ($\lambda=1.54178$ Å at 45 kV and 40 mA. SCXRD analysis was performed at the Elettra Synchrotron facility (XRD1 beamline). Data have been processed using the CrysAlisPro software package version 42.49. Detailed information on the measurement and interpretation can be found in the Supporting Information under the SCXRD section. The CIF file containing crystallographic details and structure factors is available free of charge on the Cambridge Crystallographic Data Centre website (www.ccdc.cam.ac.UK) using the identifier CCDC2304584.

Picturing of the main planes was done by a double-corrected and monochromated Themis Z scanning transmission electron microscope (Thermo Fisher Scientific) operating at 300 kV equipped through HAADF-STEM mode and integrated differential phase contrast (iDPC) STEM by using 80% coverage of a 4-segmented DF detector. The beam convergence angle was measured 16-24.0 and the probe current of 1.0 pA was used for STEM imaging. Data acquisition and analysis were done using Velox software. For this purpose, TEM samples were prepared by drop-casting a few droplets of NPs in EtOH onto the quantifoil C-support gold grids covered with single/mono layer of CVD-grown graphene to avoid beam damage. Then particles were sandwiched between the graphene layer by placing another grid on top of grids with MOF particles. The details of TEM sample preparation is available under TEM section in Supporting Information. The multislice simulation was performed using the DrProbe software package. [65] An orthogonal unit cell was first constructed with one of its axes aligned along the [1 0 0] zone axis of the experimental image. Phase gratings were calculated over a 5×5 nm area. An inner 3×3 nm square was then used for the subsequent simulation with a total thickness of 6 nm. A relatively large pixel size of 20 pm was chosen to limit computation time. All other simulation parameters were chosen to mimic the experimental setup.

Moreover, ThermoFisher Spectra Ultra (S)TEM operated at 300 kV was used for extremely low-dose imaging through the integrated Differential Phase Contrast (iDPC) STEM technique. This was performed using a Panther Detector, a segmented STEM detection system, with a probe current of 1 pA at a convergence semiangle of 10 mrad. The sample was prepared by drop-coating the particles, which were sonicated and dispersed in ethanol, onto an ultrathin carbon support film TEM grid.

SEM observation was performed with a field emission-scanning electron microscope (JEOL JSM-7401 F or Magellan 400 XHR) equipped with electron-dispersive spectroscopy (EDS). XPS analysis was conducted using a PHI-TFA XPS spectrometer (Physical Electronic Inc.). The device is equipped with an X-ray Al-monochromatic source. The vacuum level inside the measuring chamber is maintained at 10⁻⁹ mbar. The analysis region measures 0.4 mm in diameter. We conducted precise multiplex scans of the peaks with a narrow focus, utilizing a pass energy of 71.55 eV and a step size of 0.1 eV. The measurements were carried out at an angle of 45° with respect to the sample surface. Spectral processing

was performed using Multipak v8.0 (Physical Electronics Inc., Chanhassen, MN, USA). Elemental composition was determined from the XPS survey spectra, while high-energy resolution spectra of S 2p and Cu 2p, C 1s, and O 1s photoelectron peaks were subjected to curve fitting.

A Thermo-Nicolet Nexus FTIR apparatus was used equipped with a liguid-nitrogen-cooled mercury cadmium tellurium detector and a nitrogenpurged measurement chamber. The Raman spectra have been achieved by WiTeC Alpha300R Raman Imaging microscope, using 532 nm laser with 0.2 mW laser power to avoid damaging the samples with an integration time of 8 s and 10 accumulations. The sample was prepared by dissolving sample powder in IPA and drop casting on quartz slides. Thermogravimetric analyses were performed using the TAG 1750 instrument manufactured by Setaram. The powders were heated from ambient temperature to 900 °C with a heating rate of 50 °C min⁻¹ to mimic the sintering cycle used in the experiments. For the DSC, the powders were heated from ambient temperature up to 600 °C and back to ambient temperature with a heating and cooling rate of 5 °C min⁻¹ to closely measure heat flow at each temperature step. N₂ physisorption experiments were performed using a Micromeritics Tristar II 3020 at 77 K. Before the gas-sorption experiments 100 mg of MOF was washed and dried for 5 h at 100 °C.

Electrochemical Measurements and Product Analysis: A flow cell (Dioxide Materials.) with a Nafion anion exchange membrane from FORBLUE SELEMION was purchased and was modified to include a catholyte compartment. for all electrochemical measurements. The working electrode was a squared GDE coated with MOF (2.6 \times 2.6 cm, area, 6.76 cm²). Surface area correction was then applied to the calculations to exclude those portions of the electrode that were not in contact with the electrolyte, owing to modifications in the flow cell. An Iridium plate from Magneto Special Anodes B.V. and a leak-free Ag/AgCl reference electrode (Innovative Instruments LF-1-45) were used as counter electrode and reference electrode, respectively. After IR correction, all potentials were converted into those vs. RHE.

1 and 0.5 m KOH solutions were cycled through the cathode and anode compartments, respectively with a $10\,\mathrm{mL\,min^{-1}}$ flowrate. $\mathrm{CO_2}$ was bubbled from the back of the cell with a flow rate of $20\,\mathrm{mL\,min^{-1}}$ for 1.5 h to reach the electrolyte saturation. In the case of Ar flow, the same procedure was repeated.

Linear sweep voltammograms (LSV) were recorded in Ar- and CO_2 -saturated 1 M KOH at a scan rate of 5 mV s⁻¹. EIS measurements were performed for Cu–S–BDC and Cu–BDC MOFs in CO_2 -saturated 1 M KOH in the frequency range of 1 MHz to 100 mHz at OCP.

To conduct product analysis measurements, chronoamperometric measurements were conducted in 1 M KOH solution saturated with $\ensuremath{\mathsf{CO}}_2$ and Ar. The measurements were carried out at constant potentials of -0.4, -0.5, -0.6, -0.7, -0.8, -0.9, and -1 V versus the RHE. Samples of 1 mL were collected from the electrolyte reservoir at 10 min intervals to analyze liquid products using high-performance liquid chromatography (HPLC). Gas product analysis from the cathode compartment was done with GC (GC from Agilent) equipped with two thermal conductivity detectors to measure CO₂, CO, and H₂ in 2 min intervals. A standard calibration curve was made using custom gas mixture cylinders with known concentrations of product gasses in CO2 (Linde gas Benelux B.V.). The liquid products were quantified using HPLC (Agilent 1260 Infinity). 5 µL of the liquid sample was injected into two Aminex HPX 87-H columns (Bio-rad) placed in series. The column oven temperature was maintained constant at 60 °C, with a steady flow rate of 0.6 mL min⁻¹ of an aqueous 1 mM H₂SO₄ eluent, and a refractive index detector was used for product detection.

Faradaic efficiencies were calculated using Equation (1):

$$\frac{n_i NF}{jt} \tag{1}$$

where n_i represents the number of moles of the detected product, N is the number of the transferred electrons in a reaction, F is the Faradaic constant, j is the current density, and t is the time of the measurement.

www.advancedsciencenews.com

www.small-structures.com

DFT Calculations: The global optimization of the proposed MOF structure was conducted using the ab initio USPEX evolutionary algorithm methodology for crystal structure prediction. A total of 160 initial structures were considered over 10 distinct generations in the USPEX simulation. To address the limitations of the local optimizations within USPEX, which are performed using relatively weak convergence criteria and small basis sets to accelerate the evolutionary run, the ground state structures were subsequently subjected to a new local optimization process with a high cut-off and large basis sets.

The DFT computations were carried out based on the Vienna ab initio simulation package. [66–68] The generalized gradient approximation in the form of Perdew–Burke–Ernzerhof [69] functional was adopted self-consistently through the approach of the projector augmented wave [70] by Kohn–Sham electron wave functions expanded with an energy cutoff of 550 eV and the convergence criteria during the structural optimizations were set to 10^{-6} eV and 10^{-3} eV/Å for energy and force, respectively. The Monkhorst–Pack K-point [71] of the $9\times1\times5$ grid is used in the reciprocal space during the geometrical optimizations. The charge transfer between atoms is evaluated based on the Bader charge algorithm. [72] The open-source package vaspkit [73] was used for the state of density and the thermodynamics (298.15 K and 1 atm) calculations. For Gibbs free energy, the following equation was used:

$$G = H - T\Delta S = E_{DFT} + E_{ZPE} + \int_{0}^{298.15} C_{\nu} dT - T\Delta S$$
 (2)

where H refers to the enthalpy, $E_{\rm DFT}$ refers to the electronic adsorption energy, and $E_{\rm ZPE}$ signifies the zero-point vibrational energy. The calculation also includes the heat capacity ($\int_0^{298.15} C_{\nu} dT$) and entropy correction ($T\Delta S$) as the third and fourth components, respectively, derived from frequency calculations. For the gas molecules, we referenced the data from the study by Klinkova et al. [74] To mitigate the overestimation typically seen in DFT calculations, [25,75] these corrections were applied: CO₂ (0.45 eV), HCOOH (0.20 eV), and the adsorbed COOH* (0.20 eV). Finally, the adsorption energy was calculated through the following equations:

$$E_{\text{COOH}}^{ads} = E_{\text{COOH}*} - E_{\text{MOF}} - \left(E_{\text{HCOOH}} - \frac{1}{2}E_{\text{H}_2}\right) \tag{3}$$

$$E_{\text{HCOO}}^{ads} = E_{\text{HCOO}*} - E_{\text{MOF}} - \left(E_{\text{HCOOH}} - \frac{1}{2}E_{\text{H}_2}\right) \tag{4}$$

 $E_{\rm MOF}$ and $E_{\rm Molecule}$ refer to the ground state energy of the pristine MOF system and isolated molecule, respectively. Herein, we take the following reaction 5 as an example to show the calculation of Gibbs free energy variation based on the Equation (6), where e is the charge number and U is the external applied voltage; for the calculation of free energy of H^+ and e^- , the computational hydrogen electrode model^[76] was used to calculate the Gibbs free energy of proton/electron:

$$COOH* + H^{+} + e^{-} \leftrightarrow HCOOH^{+}$$
(5)

$$\Delta G = G_* + G_{\text{HCOOH}} - G_{\text{COOH}^*} - (G_{\text{H}^+} + G_{\epsilon^-})$$

$$= G_* + G_{\text{HCOOH}} - G_{\text{COOH}^*} - \left(\frac{1}{2}G_{\text{H}_2} - eU\right)$$
(6)

Supporting Information

Supporting Information is available from the Wiley Online Library or from the author.

Acknowledgements

The Elettra Synchrotron (CNR Trieste, Italy) is acknowledged for granting beamtime at the single-crystal diffraction beamline XRD1 (Proposal ID 20230540). S.C. gratefully thanks Prof. Bettina V. Lotsch for supporting

his participation to this work. N.K. and P.D. acknowledge the computational resources provided by Dutch Research Organization NWO (Snellius@Surfsara) and DelftBlue supercomputer provided by Delft High-Performance Computing Centre (https://www.tudelft.nl/dhpc). K.R. thanks Agnieszka Kooijman, J.C. Brouwer, R.W.A. Hendrikx, and Dr. G.A. Filonenko at the Department of Materials Science and Engineering and J.W. Blake at the Department of Process and Energy of Delft University of Technology for their technical support, assistance with experiments, and their valuable ideas and insights during this project.

Conflict of Interest

The authors declare no conflict of interest.

Author Contributions

Khatereh Roohi executed the experimental work, while Nabil Khossossi conducted the DFT calculations. Khatereh Roohi and Mohammad Soleimani synthesized the materials. Stefano Canossa carried out the SCXRD measurements and provided the corresponding interpretations. Majid Ahmadi, Ewout van der Veer, and Ali Kosari performed TEM imaging and structure refinement. Prasad Gonugunta conducted the BET, TGA, and FTIR experiments, and Seyedamirhossein Mohseni Armaki performed the Raman measurements. Prasaanth Ravi Anusuyadevi and Mahinder Ramdin contributed to the product analyses. Peyman Taheri conceptualized and supervised the work, and Poulumi Dey supervised the DFT calculations. Khatereh Roohi, Nabil Khossossi, and Peyman Taheri co-wrote the paper, which was edited by J.M.C. Mol. All authors discussed the results, read, and provided comments on the manuscript.

Data Availability Statement

Research data are not shared.

Keywords

 ${\rm CO_2}$ electrochemical reduction, conductivity, Cu–S planes, formate selectivity, metal–organic frameworks

Received: April 11, 2025 Revised: May 31, 2025 Published online: July 7, 2025

- [1] M. Li, H. Wang, W. Luo, P. C. Sherrell, J. Chen, J. Yang, Adv. Mater 2020, 32, 2001848.
- [2] M. Amiri, M. Ahmadi, N. Khossossi, P. Gonugunta, K. Roohi, B. Kooi, M. Ramdin, P. Ravi Anusuyadevi, T. Tatte, N. Kongi, A. Vanetsev, P. Dey, P. Taheri, J. Catal. 2025, 116022.
- [3] X. Chen, J. Chen, N. M. Alghoraibi, D. A. Henckel, R. Zhang, U. O. Nwabara, K. E. Madsen, P. J. A. Kenis, S. C. Zimmerman, A. A. Gewirth, *Nat. Catal.* 2021, 4, 20.
- [4] S. Zhang, P. Kang, T. J. Meyer, J. Am. Chem. Soc. 2014, 136, 1734.
- [5] J. Ding, H. Bin Yang, X. L. Ma, S. Liu, W. Liu, Q. Mao, Y. Huang, J. Li,T. Zhang, B. Liu, *Nat. Energy* 2023, 8, 1386.
- [6] P. Gonugunta, K. Roohi, M. Soleimani, P. R. Anusuyadevi, P. Taheri, M. Ramdin, Ind. Eng. Chem. Res. 2025.
- [7] D. Gao, H. Zhou, F. Cai, J. Wang, G. Wang, X. Bao, ACS Catal. 2018,
- [8] J. Y. T. Kim, C. Sellers, S. Hao, T. P. Senftle, H. Wang, Nat. Catal. 2023, 6, 1115.

www advancedsciencenews com

www.small-structures.com

- [9] D. H. Nam, P. De Luna, A. Rosas-Hernández, A. Thevenon, F. Li, T. Agapie, J. C. Peters, O. Shekhah, M. Eddoudi, E. H. Sargent, Nat. Mater. 2020, 19, 266.
- [10] H. Xu, D. Rebollar, H. He, L. Chong, Y. Liu, C. Liu, C.-J. Sun, T. Li, J. V. Muntean, R. E. Winans, D.-J. Lui, T. Xu, Nat. Energy 2020, 5, 623.
- [11] X. Li, X. Wu, X. Lv, J. Wang, H. B. Wu, Chem. Catal. 2022, 2, 262–291.
- [12] W. Yang, K. Dastafkan, C. Jia, C. Zhao, Adv. Mater. Technol. 2018, 3, 1700377.
- [13] Q. Lu, F. Jiao, Nano Energy 2016, 29, 439.
- [14] B. Zhang, Y. Jiang, M. Gao, T. Ma, W. Sun, H. Pan, Nano Energy 2021, 80, 105504.
- [15] Y. Y. Birdja, E. Pérez-Gallent, M. C. Figueiredo, A. J. Göttle, F. Calle-Vallejo, M. T. Koper, Nat. Energy 2019, 4, 732.
- [16] W. Yang, Q. Mo, Q. T. He, X. P. Li, Z. Xue, Y. L. Lu, J. Chen, K. Zheng, Y. Fan, G. Li, C.-Y. Su, Angew. Chem., Int. Ed. 2024, 63, e202406564.
- [17] Y. Hori, K. Kikuchi, S. Suzuki, Chem. Lett. 1985, 14, 1695.
- [18] F. Li, Y. C. Li, Z. Wang, J. Li, D. H. Nam, Y. Lum, M. Luo, X. Wang, A. Ozden, S.-F. Hung, B. Chen, Y. Wang, J. Wicks, Y. Xu, Y. Li, C. M. Gabardo, C.-T. Dinh, Y. Wang, T.-T. Zhuang, D. Sinton, E. H. Sargent, *Nat. Catal.* 2020, 3, 75.
- [19] D. Cheng, Z. J. Zhao, G. Zhang, P. Yang, L. Li, H. Gao, S. Liu, X. Chang, S. Chen, T. Wang, G. A. Ozin, Z. Liu, J. Gong, Nat. Commun. 2021, 12, 395.
- [20] R. Kortlever, J. Shen, K. J. P. Schouten, F. Calle-Vallejo, M. T. Koper, J. Phys. Chem. Lett. 2015, 6, 4073.
- [21] D. Voiry, H. S. Shin, K. P. Loh, M. Chhowalla, Nat. Rev. Chem. 2018, 2, 0105.
- [22] A. A. Peterson, J. K. Nørskov, J. Phys. Chem. Lett. 2012, 3, 251.
- [23] J. Pérez-Ramrez, N. López, Nat. Catal. 2019, 2, 971.
- [24] T. Shinagawa, G. O. Larrazábal, A. J. Martn, F. Krumeich, J. Pérez-Ramrez, ACS Catal. 2018, 8, 837.
- [25] J. S. Yoo, R. Christensen, T. Vegge, J. K. Nørskov, F. Studt, ChemSusChem 2016, 9, 358.
- [26] C. H. van Oversteeg, M. T. Rosales, K. H. Helfferich, M. Ghiasi, J. D. Meeldijk, N. J. Firet, P. Ngene, C. de Mello Donega, P. E. de Jongh, Catal. Today 2021, 377, 157.
- [27] Y. Deng, Y. Huang, D. Ren, A. D. Handoko, Z. W. Seh, P. Hirunsit, B. Siang Yeo, ACS Appl. Mater. interfaces 2018, 10, 28572.
- [28] L. Majidi, A. Ahmadiparidari, N. Shan, S. N. Misal, K. Kumar, Z. Huang, S. Rastegar, Z. Hemmat, X. Zou, P. Zapol, J. Cabana, L. A. Curtiss, A. Salehi-Khojin, Adv. Mater 2021, 33, 2004393.
- [29] J. Liu, D. Yang, Y. Zhou, G. Zhang, G. Xing, Y. Liu, Y.Ma, O. Terasaki, S. Yang, L. Chen, Angew. Chem., Int. Ed. 2021, 60, 14473.
- [30] M. Bonneau, C. Lavenn, J. J. Zheng, A. Legrand, T. Ogawa, K. Sugimoto, F.-X. Coudert, R. Reau, S. Sakaki, K.-I. Otake, S. Kitagawa, *Nat. Chem.* 2022, 14, 816.
- [31] L. Wang, J. Mao, G. Huang, Y. Zhang, J. Huang, H. She, C. Liu, H. Liu, Q. Wang, Chem. Eng. J. 2022, 446, 137011.
- [32] C. A. Downes, S. C. Marinescu, ChemSusChem 2017, 10, 4374.
- [33] L. Sun, M. G. Campbell, Angew. Chem., Int. Ed. 2016, 55, 3566.
- [34] L. S. Xie, G. Skorupskii, Chem. Rev. 2020, 120, 8536.
- [35] L. Sun, T. Miyakai, S. Seki, J. Am. Chem. Soc. 2013, 135, 8185.
- [36] A. Pathak, J. W. Shen, M. Usman, L. F. Wei, S. Mendiratta, Y. S. Chang, B. Sainbileg, C.-M. Ngue, R.-S.Chen, M. Hayashi, T.-T. Luo, F.-R. Chen, K.-H Chen, T.-W. Tseng, L.-C. Chen, K.-L. Lu, Nat. Commun. 2019, 10, 1721.
- [37] P. Ayala, S. Naghdi, S. P. Nandan, S. N. Myakala, J. Rath, H. Saito, P. Guggenberger, L. Lakhanlal, F. Kleitz, M. C. Toroker, A. Cherevan, D. Eder, Adv. Energy Mater. 2023, 13, 2300961.
- [38] H. Rabl, S. N. Myakala, J. Rath, B. Fickl, J. S. Schubert, D. H. Apaydin, D. Eder, Commun. Chem. 2023, 6, 43.
- [39] B. Jin, J. Gao, Y. Zhang, M. Shao, Smart Mol. 2024, 2, e20230026.

- [40] X. Kang, L. Li, A. Sheveleva, X. Han, J. Li, L. Liu, F. Tuna, E. J. L. McInnes, B. Han, S. Yang, M. Schroder, *Nat. Commun.* 2020, 11, 5464.
- [41] C. G. Carson, K. Hardcastle, J. Schwartz, X. Liu, C. Hoffmann, R. A. Gerhardt, R. Tannenbaum, Synthesis and structure characterization of copper terephthalate metal-organic frameworks. EurJIC, Wiley Online Library 2009, 2338-2343.
- [42] D. Head, C. McCarty, Tetrahedron Lett. 1973, 14, 1405.
- [43] M. Sajjad, M. B. Tahir, I. Mubeen, M. R. Kabli, J. Inorg. Organomet. Polym. Mater. 2020, 30, 3965.
- [44] G. Zhan, L. Fan, F. Zhao, Z. Huang, B. Chen, X. Yang, S. Zhou, Adv. Funct. Mater. 2019, 29, 1806720.
- [45] T. Ghanbari, F. Abnisa, W. M. A. W. Daud, Sci. Total Environ. 2020, 707, 135090.
- [46] S. H. Chaki, J. Tailor, M. Deshpande, Mater. Sci. Semicond. Proc. 2014, 27, 577.
- [47] L. Sun, Y. Zhao, Y. Shang, C. Sun, M. Zhou, Chem. Phys. Lett. 2017, 689. 56.
- [48] L. Debbichi, M. Marco de Lucas, J. Pierson, P. Kruger, J. Phys. Chem. C 2012, 116, 10232.
- [49] I. Mnguez-Bacho, M. Courté, C. Shi, D. Fichou, Mater. Lett. 2015, 159, 47.
- [50] P. M. Shanthi, P. J. Hanumantha, K. Ramalinga, B. Gattu, M. K. Datta, P. N. Kumta, J. Electrochem. Soc. 2019, 166, A1827.
- [51] M. Usman, S. Mendiratta, S. Batjargal, G. Haider, M. Hayashi, N. Rao Gade, J. Chen, Y. Chen, K. Lu, ACS Appl. Mater. Interfaces 2015, 7, 22767.
- [52] E. A. Dolgopolova, A. J. Brandt, O. A. Ejegbavwo, A. S. Duke,
 T. D. Maddumapatabandi, R. P. Galhenage, B. W. Larson,
 O. G. Reid, S. C. Ammal, A. Heyden, M. Chandrashekhar,
 V. Stavila, D. A. Chen, N. B. Shust, J. Am. Chem. Soc. 2017, 139, 5201.
- [53] A. S. Duke, E. A. Dolgopolova, R. P. Galhenage, S. C. Ammal, A. Heyden, M. D. Smith, D. A. Chen, N. B. Shustova, J. Phys. Chem. C 2015, 119, 27457.
- [54] S. S. Park, E. R. Hontz, L. Sun, C. H. Hendon, A. Walsh, T. Van Voorhis, M. Dinca, J. Am. Chem. Soc. 2015, 137, 1774.
- [55] M. L. Aubrey, B. M. Wiers, S. C. Andrews, T. Sakurai, S. E. Reyes-Lillo, S. M. Hamed, C. Yu, L. E. Darago, J. A. Mason, J. Baeg, F. Grandjean, G. J. Long, S. Seki, J. B. Neaton, P. Yang, J. R. Long, *Nat. Mater.* 2018, 17, 625.
- [56] T. Hu, W. Zhong, T. Zhang, W. Wang, Z. Wang, Nat. Commun. 2023, 14, 7092.
- [57] B. G. Diamond, L. I. Payne, C. H. Hendon, Commun. Chem. 2023, 6, 67.
- [58] K. T. Butler, C. H. Hendon, A. Walsh, ACS Appl. Mater. Interfaces 2014, 6, 22044.
- [59] C. Suppaso, R. Nakazato, S. Nakahata, Y. Kamakura, F. Ishiwari, A. Saeki, D. Tanaka, K. Kamiya, K. Maeda, Adv. Funct. Mater. 2024.
- [60] G. L. De Gregorio, T. Burdyny, A. Loiudice, P. Iyengar, W. A. Smith, R. Buonsanti, ACS Catal. 2020, 10, 4854-4862.
- [61] T. Zhang, Z. Li, X. Lyu, J. Raj, G. Zhang, H. Kim, X. Wang, S. Chae, L. Lemen, V. N. Shanov, J. Wu, J. Electrochem. Soc. 2022, 169, 104506.
- [62] M. Van den Bossche, C. Rose-Petruck, H. Jonsson, J. Phys. Chem. C 2021, 125, 13802.
- [63] Z. Yang, H. Wang, X. Fei, W. Wang, Y. Zhao, X. Wang, X. Tan, Q. Zhao, H. Wang, J. Zhu, L. Zhou, H. Ning, M. Wu, Appl. Catal. B Environ. 2021, 298, 120571.
- [64] B. Ren, G. Wen, R. Gao, D. Luo, Z. Zhang, W. Qiu, Q. Ma, X. Wang, Y. Cui, L. Ricardez-Sandoval, A. Yu, Z. Chen, *Nat. Commun.* 2022, 13, 2486.
- [65] J. Barthel, Ultramicroscopy 2018, 193, 1-11.
- [66] G. Kresse, J. Hafner, Phys. Rev. B 1993, 48, 13115.
- [67] G. Kresse, J. Furthmüller, Comp. Mater. Sci. 1996, 6, 15.
- [68] G. Kresse, J. Furthmüller, Physical review B 1996, 54, 11169.
- [69] J. P. Perdew, K. Burke, M. Ernzerhof, Phys. Rev. Lett. 1996, 77, 3865.



www.advancedsciencenews.com www.small-structures.com

- [70] P. E. Blöchl, Phys. Rev. B 1994, 50, 17953.
- [71] M. Methfessel, A. Paxton, Phys. Rev. B 1989, 40, 3616.
- [72] G. Henkelman, A. Arnaldsson, H. Jónsson, Comp. Mater. Sci. 2006, 36, 354.
- [73] Q. Gong, P. Ding, M. Xu, X. Zhu, M. Wang, J. Deng, *Nat. Commun.* 2019, 10, 2807.
- [74] A. Klinkova, P. De Luna, C. T. Dinh, O. Voznyy, E. M. Larin, E. Kumacheva, E. H. Sargent, ACS Catal. 2016, 6, 8115.
- [75] R. Christensen, H. A. Hansen, T. Vegge, Catal. Sci. Technol. 2015, 5, 4946.
- [76] J. K. Nørskov, J. Rossmeisl, A. Logadottir, L. Lindqvist, J. R. Kitchin, T. Bligaard, H. Jonsson, J. Phys. Chem. B 2004, 108, 17886.